In-situ Inspection of Laser Powder Bed Fusion Ti-6AL-4V Additive Manufacturing using an Infrared Sensor

Joseph N. Zalameda[1], Samuel J. A. Hocker[1], Peter W. Spaeth[1] and Brandon Widener[2]

[1]NASA Langley Research Center, Hampton, VA 23681-2199, USA
[2]Analytical Mechanics Associates, Hampton, VA 23666, USA

ABSTRACT

Additive manufacturing of metallic structures requires nondestructive evaluation (NDE) to ensure part quality. For large parts with complex geometries, post build NDE can be challenging using conventional techniques such as ultrasound or X-ray computed tomography (CT). In-situ NDE offers some advantages during the build process such as layer by layer inspection, potential to correct for detected defects, and stoppage of the build if significant defects occur. In-situ NDE can provide input to validate defect prediction models that are necessary to predict the fatigue life performance of a built part thus allowing a computationally informed framework for part certification. In this work we utilize a high speed near infrared (NIR) camera within a configurable additive testbed (CAT) system for the in-situ inspection. The NIR camera is co-axially aligned with the laser within the CAT system and records the melt pool and the transient cool down areas after solidification of Ti-6Al-4V laser powder bed fusion builds. Detection of defects, layer by layer, consists of processing the thermal data for differences in the transient cool down temperature responses after solidification. The thermal data will be analyzed with a focus on the detection of lack of fusion porosity. The results are compared to X-ray CT for validation.

Keywords: additive manufacturing, lack of fusion porosity, in-situ near infrared imaging, laser co-axial near infrared imaging, data reconstruction, melt pool imaging, X-ray computed tomography

1. INTRODUCTION

In-situ nondestructive evaluation during the additive manufacturing (AM) process offers many advantages. For example, the built part can be delivered in addition to the inspection data, thus potentially saving the extra step of performing an inspection after the build. Another advantage is during the build, since the inspection could be performed layer by layer, if defects are detected the build process can be stopped and a repair can be implemented or if the defect is significant the entire build process can be stopped to save time and material costs.

In this study, we extend our previous work [1] and apply our technique for the detection of lack of fusion porosity using a near infrared (NIR) camera that is optically aligned with a laser to perform the in-situ inspection. The laser is scanned over a surface and used to melt the metal powder layer by layer in a laser powder bed fusion (LPBF) process. Defects such as lack of fusion can affect the mechanical part performance and the formation of these defects can be attributed to the processing conditions [2-5]. In this work, we describe a Configurable Additive Testbed (CAT) system which was used to vary the processing parameters during LPBF AM.

The CAT system is a custom developed AM system that is comprised of an enclosed environmental chamber which has been modified to conduct LPBF experiments [1,6]. The CAT is used to test various process parameters and materials and can be custom configured with a variety of sensors, such as NIR cameras, for in-situ NDE. The NIR cameras are co-axially aligned optically with the laser and thus allow for high resolution imaging of the melt pool and surrounding areas. The thermal data is obtained during a LPBF process and of particular interest is lack of fusion porosity which can result from build conditions with relatively lower laser power for a given laser scanning speed and laser beam focus. The NIR

*joseph.n.zalameda@nasa.gov; phone 1 757-864-4793; fax 1 757-864-4914; http://nde.larc.nasa.gov

measured melt pool and cooling areas are processed to detect thermal anomalies that can be related to lack of fusion pores. The results are compared to X-ray computed tomography (CT).

2. ADDITIVE MANUFACTURING AND MEASUREMENT SYSTEM DESCRIPTION

2.1 Configurable Additive Testbed (CAT)

The CAT system is comprised of an enclosed environmental chamber that has been modified to conduct LPBF experiments with a variety of sensors and multiple view port windows for various camera configurations. Shown in Figures 1(a) and 1(b) are a picture of the CAT system and drawing respectively. The CAT is configured with an environmental chamber such that the builds are conducted with <10 ppm O_2, measured using a PureAire[1] trace oxygen analyzer. The crossflow velocity is measured to be 90 mm/s. A SCANLAB GmbH IntelliScan III 20[1] galvanometer head is driven by a SCANLAB RTC61[1] control board and an IPG Photonics[1] modulated continuous emission 1070 nm Gaussian laser with a maximum power of 1 kW to conduct the welds. A Jenoptik F-Theta[1] lens with a 255 mm working distance is used for a near uniform laser spot diameter of 40 µm across a 25.4 x 25.4 mm build area. The in-line (coaxial to the laser heat source) camera sensor setups are shown in Figure 2. The setup shows beam splitter #2 which splits the light for the two NIR cameras. Camera #1 is configured with a 725 nm bandpass filter with full width half max (FWHM) band pass from 700 to 750 nm. Camera #2 is configured with a 900 nm bandpass filter with FWHM band pass from 875 to 925 nm. Both camera fields of view follow the laser path using the SCANLAB GmbH[1] camera adapter that consists of a focusing objective (configured with 1070 nm notch filters) and a beam splitter #1. This coaxial method is used to obtain the highest resolution imagery of the melt process. The beam splitter #1 also separates the 1070 nm laser beam from the NIR wavelengths that are measured by the cameras. The in-line cameras used are the Photron Fastcam Nova S6[1]. These cameras have a CMOS sensor, a 20 x 20 um pixel pitch, a 1024 x 1024 pixel array, a dynamic range of 12 bits, and a maximum frame rate of 6,400 Hz at full pixel resolution. The fields of view of the cameras are configured to capture 512 x 512 pixels a 2,000 Hz frame rate was used. The camera integration time was set to 10 us. The cameras are triggered simultaneously in concert with the mirror position and therefore the exact position of the laser is known within the camera imagery. For this study the data from camera #1 with the 725 nm filter were analyzed due to good signal to noise with minimal pixel intensity saturation.

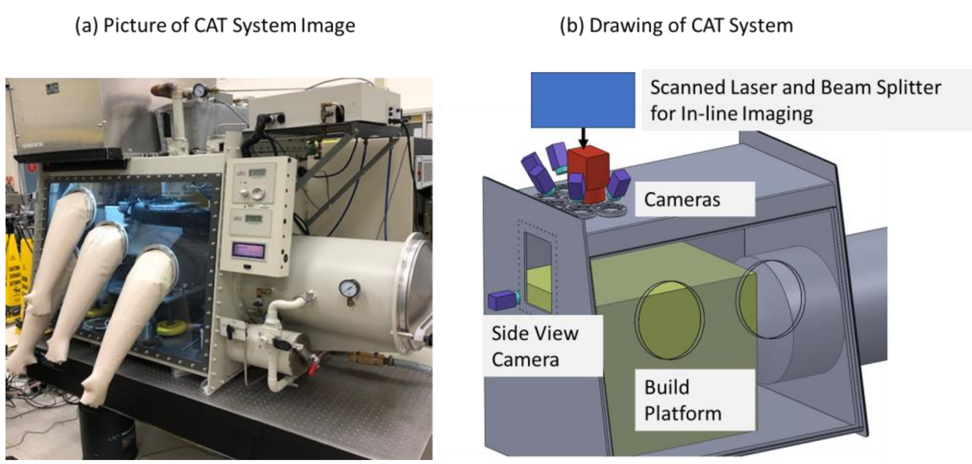

Figure 1: CAT system setup (a) picture of system and (b) drawing of test setup.

[1] Specific vendor and manufacturer names are used only to accurately describe the test hardware or software. The use of vendor and manufacturer names does not constitute an official endorsement, either expressed or implied, by the National Aeronautics and Space Administration nor does it imply that the specified equipment or software is the best available.

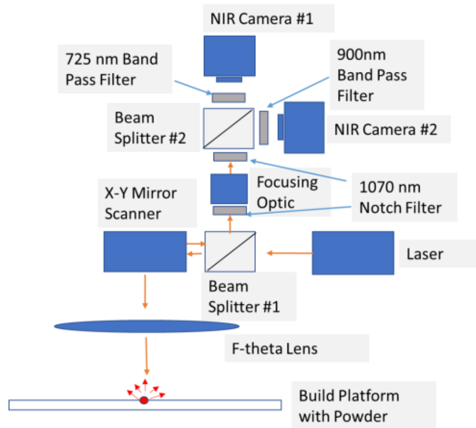

Figure 2: In-line NIR camera setup.

3. TI-6AL-4V AM BUILT SAMPLES

3.1 Ti-6Al-4V Disk Sample Description

Two sets of Ti-6Al-4V disk samples were fabricated using the LPBF process with different processing parameters. The samples were P1*a*, P1*b*, P1*c*, P2*a*, P2*b*, and P2*c*. The processing parameters for the P1 samples were a laser power of 350 Watts, scanning speed of 1400 mm/sec, and hatch spacing of 0.1 mm. The processing parameters for the P2 samples were a laser power of 240 Watts, scanning speed of 1400 mm/sec, and hatch spacing of 0.1 mm. The differences between samples *a*, *b* and *c* designations are due to the chamber inert gas crossflow in relation to the meandering laser scanning path as described in [6] wherein for *a*, the layer-wise hatch progression pattern is both with and against the crossflow, *b* is the layer-wise hatch progression pattern with the crossflow, and *c* is the layer-wise hatch progression pattern against the crossflow. The disk sample diameters were approximately 25.4 mm with thicknesses of approximately 6.35 mm. Each build layer was approximately 50 microns and therefore 126 layers was necessary for the given thickness. A representative disk sample is shown in Figure 3. The higher power P1 samples were expected to be more consolidated with less pores as compared to the lower power P2 samples which would have lack of fusion pores due to the lower energy delivered. This is clearly seen in Figure 4 showing the comparison of the cross section X-ray CT slices that were taken from left to right at the sample's maximum width. As shown in Figure 4, the P1 samples processed with laser power equal to 350 Watts reveal very low porosity with some very small lack of fusion or keyhole pores. The P2 disk samples reveal larger areas of voids (dark spots) which indicates lack of fusion pores.

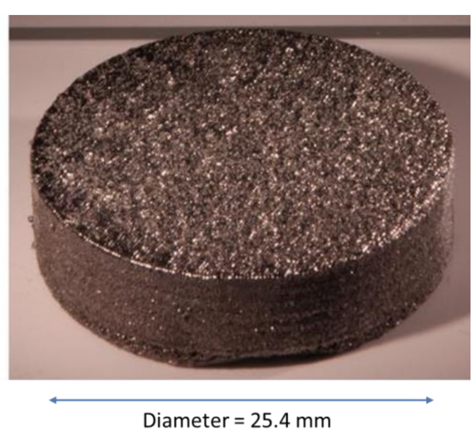

Figure 3: Photograph of representative Ti-6Al-4V disk sample.

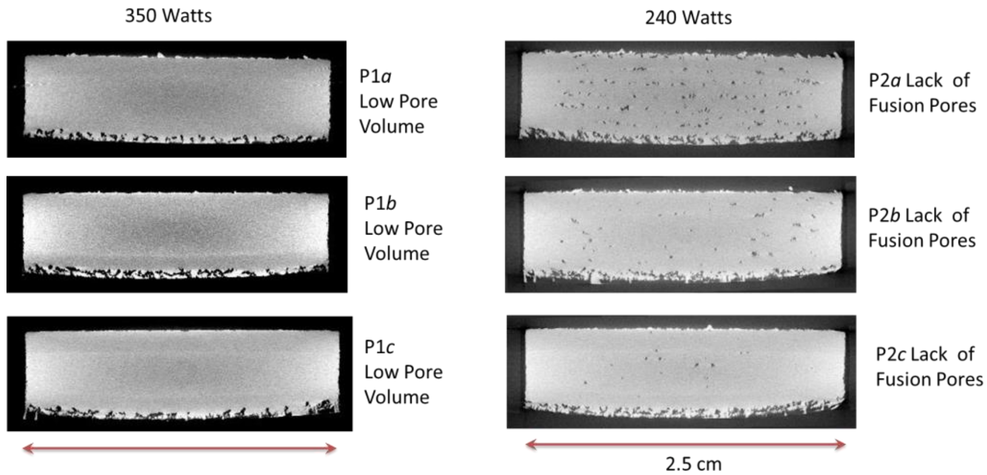

Figure 4: Comparison of X-ray CT cross section slices revealing porosity indications within each disk sample.

4. IN-SITU NIR THERMAL IMAGING AND DATA RECONSTRUCTION

4.1 NIR Imaging

The NIR camera #1 is aligned co-axially with the laser and this allows for high resolution thermal imaging during the AM build, with a resolution of approximately 10 microns/pixel. The camera frame rate was set to 2 kHz with a 10 *us* integration time. The integration time was necessary to minimize saturation with adequate capture of the melt pool area, semi-solid regions, and solid cool down areas [1]. The laser XY position was recorded for a given acquired camera image. The camera imagery can then be reconstructed, for a known XY position, to produce a series of images that captures the laser generated melt pool along the entire build path for a given layer.

4.2 NIR Image Data Reconstruction

The data reconstruction procedure is defined in the block diagram shown in Figure 5. The acquired NIR thermal images, for a known XY position is processed using a median blur 3x3 filter and rotated wherein the orientation of the melt pool and semi-solid regions are horizontal. The laser XY scanning positions are also rotated to be horizontal as shown in Figure 6. The rotated NIR imagery is then resampled to a 256 x 256 pixel array size and a region of interest (ROI) of 6 x 256 pixels is selected which covers the melt pool area, semi-solid regions, and solid cool down areas. The ROI is necessary to remove spatter ejecta which can distort the thermal profile. For each ROI image, the image center is determined from the maximum along the length and width and is mapped to the XY laser position as an overlay onto the entire layer scan path image.

For example, the scan path image dimensions used were 2750 x 2750 pixels and the number of images for a given layer are typically around 7200 frames. This creates an enormous data file and therefore the scan path image with the NIR image overlay is resampled down to 675 x 675. The scan path image stack represents the entire movement of melt pool, semi-solid, and cool down regions for a given layer. The scan path image stack can then be processed where the maximum for every pixel is aligned into a new image stack where each image now represents the temperature versus time cool down responses. The camera frame rate is 2 kHz and therefore each reconstructed image represents 0.0005 second time steps and it was observed that 5 frames captured the entire cool down profile as shown in Figure 7 (data from sample P2*b*). Since the temporal sampling was sparse, principal component analysis [7] was not used to detect defects. Suspect areas of defects were detected if the underlying substructure affects the surface cool down revealing residual hot spots [8]. These hot spots can be seen in the 0.0010 and 0.0015 second images in Figure 7. For the timescales in this study, it is expected that near surface defects would affect the cool down during melt pool solidification given each layer's thickness of approximately 50 microns [1]. Spatter surface defects could also cause hot spots again due to the lack of fusion of the powder [6,9]. For a comparison to X-ray CT, the pixel intensity counts were tracked for the 0.0010 and 0.0015 second images for each of the six disk samples studied at build layer 63 (center layer). An example is shown in Figure 8, for the

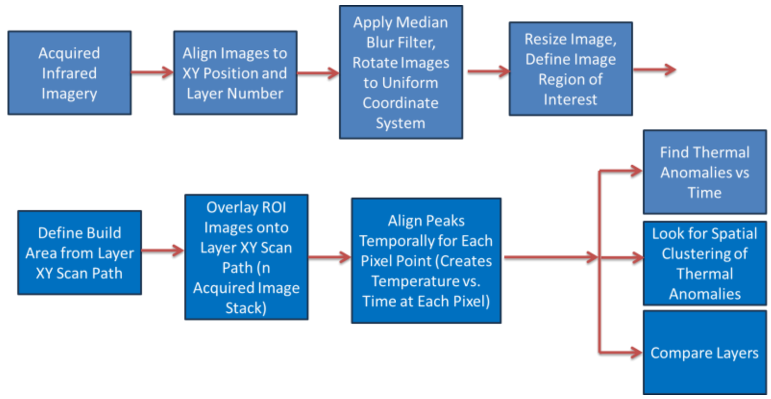

Figure 5: Data processing for NIR image reconstruction to spatial cool down temperature vs. time.

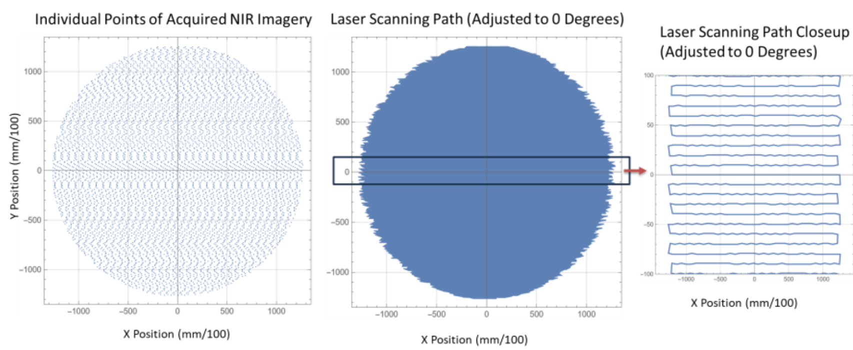

Figure 6: Scanning configuration for a given layer with individual points shown where infrared images were acquired.

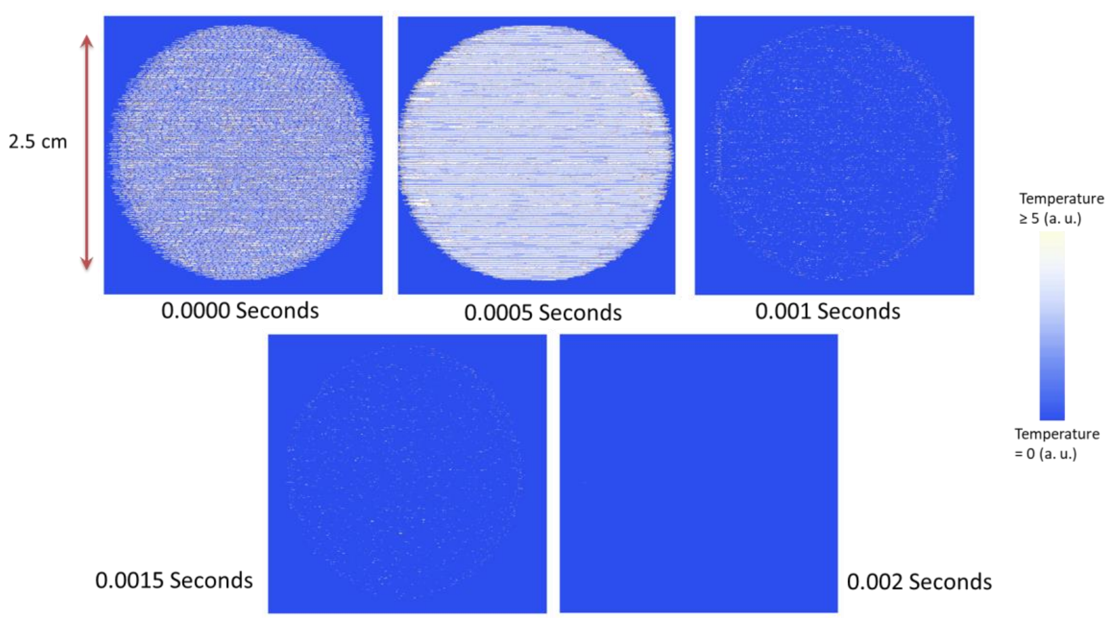

Figure 7: Reconstructed thermal cool down imagery versus time (sample P2*b*).

P1*c* and P2*c* samples which represents two processing powers of 350 and 240 Watts respectively. The 0.001 seconds thermal cool down images and pixel intensity image histograms are plotted alongside the images in Figure 8. As shown in Figure 8, the lower power of 240 Watt has considerably more thermal anomalies (hot spots) as compared to the 350 Watt image. This can be confirmed with the X-ray CT results shown in Figure 4 where the P1*c* image appears to be more consolidated with less pores as compared to the P2*c* image where larger lack of fusion pores are clearly visible. The comparison for all six disks is shown in Table 1, where the total number of pixels over a threshold are counted. For example, for the 0.0010 second images the threshold was set to a value of 1.0 and for the 0.0015 second images the threshold was set to a value of 0.1. Table 1, indicates consistently, for the lower laser powers there are more thermal anomalies detected as compared to the higher laser power which can be attributed to the presence of lack of fusion pores. It is interesting to note that from the X-ray CT results, the P2*a* disk had more lack of fusion pores as compared to the P2*b* and P2*c* disks, however the number of detected thermal anomalies was less. Alternatively, the P1*b* disk had a significant number of detected thermal anomalies whereas the X-ray CT indicated minimal pores. This may be due to the hatch progression pattern which was with the gas flow and therefore spatter ejecta accumulated in regions just before melting (also in the P2*b* disk that had the most thermal anomalies overall). It is important to note only one layer (layer 63) of in-situ thermal data was analyzed. A more thorough study of all the layers (126 total) for each of the six disk samples would be the next step for further comparisons of the laser power effects, gas cross flow relations, and allow for selection of optimal thermal thresholds. In addition, the spatial location of the thermal anomalies to the X-ray CT would require an alignment between the different coordinate systems and this would further validate this technique for the detection of lack of fusion porosity. The registration of the in-situ thermal and the X-ray CT data, volumetrically, would also allow for relating the clustered thermal anomalies to the larger lack of fusion pores.

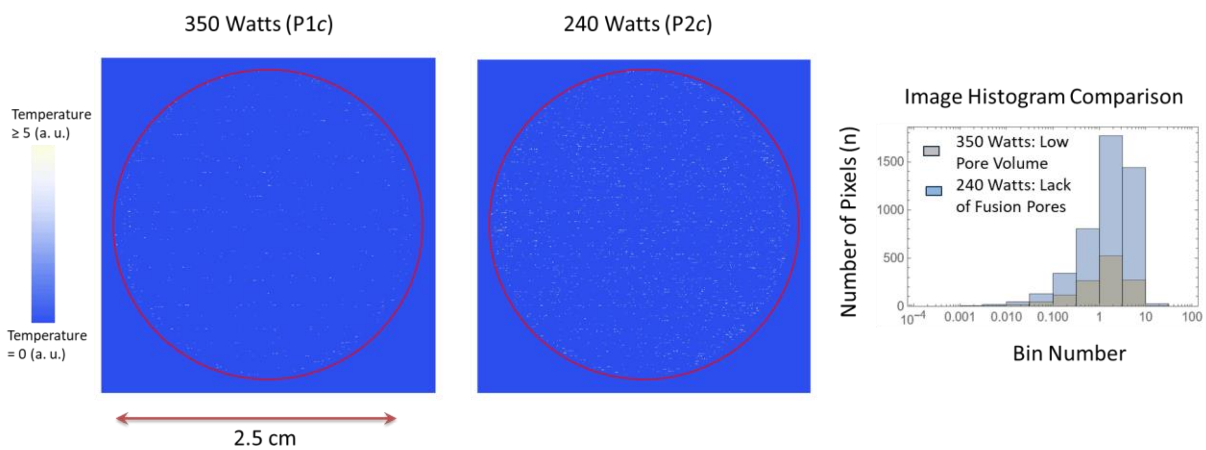

Figure 8: P1*c* and P2*c* thermal cool down images at 0.0010 seconds with image histogram comparing pixel intensities.

Table 1: Comparison of thermal cool down indications for crossflow and two different laser powers.

Sample ID	Power (Watts)	Layer Hatch Pattern Progression in Relation to Inert Gas Crossflow	Number of Thermal Anomalies @0.0010 Seconds (Threshold ≥ 1)	Number of Thermal Anomalies @0.0015 Seconds (Threshold ≥ .1)	X-ray CT Imaging Results
P1*a*	350	Both Against and With	770	56	Low Pore Volume
P1*b*	350	With	2127	90	Low Pore Volume
P1*c*	350	Against	800	56	Low Pore Volume
P2*a*	240	Both Against and With	1350	71	Lack of Fusion Pores
P2*b*	240	With	3605	127	Lack of Fusion Pores
P2*c*	240	Against	3227	107	Lack of Fusion Pores

5. CONCLUSIONS

A methodology is presented to detect thermal cool down anomalies using in-situ infrared thermal imaging captured during the LPBF build. Table 1 results show a consistent trend of more thermal cool down anomalies for the lower laser power as compared to the higher laser power. From the X-ray CT results, it is shown the lower laser power samples had the larger lack of fusion pores. Also, Table 1 results show more thermal anomalies with the layer hatch pattern progressing with or in the same direction of the inert gas crossflow and this can be due to the spatter ejecta accumulating in regions just before melting. A more thorough study of all the layers (126 total) for each of the six disk samples would be the next step for further comparison and validation. In addition, the spatial location of the thermal anomalies to the X-ray CT would require an alignment between the different coordinate systems volumetrically and this would further validate this technique for the detection and characterization of lack of fusion porosity.

ACKNOWLEDGEMENTS

The authors would like to acknowledge William P. Sommers of the Nondestructive Evaluation Sciences Branch NASA Langley for the X-ray CT measurements. Also, this work was done under the NASA Aeronautics Research and Mission Directorate's Transformational Tools and Technologies (TTT) AM project.

REFERENCES

[1] Zalameda, J. N.. Hocker, S. J., Spaeth, P. W., Widener, B., "Near-infrared in-situ measurements for the detection of keyhole porosity in autogenous Ti-6Al-4V welds," Proc. SPIE 13047, Thermosense: Thermal Infrared Applications XLVI, 130470X (7 June 2024); https://doi.org/10.1117/12.3014612

[2] Yap, C.Y., Chua, C.K., Dong, Z.L., Liu, Z.H., Zhang, D.Q., Loh, L.E., and Sing, S.L., Review of Selective laser melting: Materials and applications, Applied Physics Reviews 2, 041101 (2015); doi:10.1063/1.4935926.

[3] Everton, S., Hirsch, M., Stravroulakis, P., Leach, R., and Clare, A., "A Review of in-situ process monitoring and in-situ metrology for metal additive manufacturing", AI, Materials & Design, vol. 95, April 2016.

[4] Soltani-Tehrani, A., Shrestha, R., Phan, N., Seifi, M., & Shamsaei, N. (2021). Establishing specimen property to part performance relationships for laser beam powder bed fusion additive manufacturing. International Journal of Fatigue, 151, 106384.

[5] Hocker, S.J.A., Richter, B., Spaeth, P.W., Kitahara, A.R., Zalameda, J.N., Glaessgen, E.H., 2023. A Point Field Driven Approach to Process Metrics Based on Laser Powder Bed Fusion Additive Manufacturing Models and In-Situ Process Monitoring. JMR. https://doi.org/10.1557/s43578-023-00953-7.

[6] Hocker, S.J.A., Kitahara, A.R., Richter, B. et al. A Novel Additive Manufacturing Process Metric for Predicting Spatter-Related Porosity in Laser Powder Bed Fusion. Integr Mater Manuf Innov 14, 53–73 (2025). https://doi.org/10.1007/s40192-024-00376-0.

[7] Rajic, N., "Principal Component Thermography for Flaw Contrast Enhancement and Flaw Depth Characterisation in Composite Structures", Composite Structures, Vol. 58, pp. 521--528, (2002).

[8] Zalameda, Joseph N., Eric R. Burke, Robert A. Hafley, and Christopher S. Domack. "System and method for in-situ characterization and inspection of additive manufacturing deposits using transient infrared thermography." U.S. Patent 11,027,332, issued June 8, 2021.

[9] Khairallah, S. A., Anderson, A. T., Rubenchik, A. and King, W. E., "Acta Materialia Laser powder-bed fusion additive manufacturing: Physics of complex melt flow and formation mechanisms of pores, spatter, and denudation zones," Acta Mater., vol. 108, pp. 36–45, 2016, doi: 10.1016/j.actamat.2016.02.014.